Check for updates

Advanced Materials

ADVANCED MATERIALS
www.advmat.de

RESEARCH ARTICLE

Grain-Boundary-Facilitated Palladium Hydride Formation Enables Humidity-Tolerant Catalytic Hydrogen Sensing

Bingxin Yang[1] | Sampreeti Bhattacharya[2] | Heng Liu[3] | Michael A. Pence[1,4] | K. A. U. Madhushani[1] | Bobby G. Duersch[5] | Linfeng Yu[6] | Hyoju Park[2] | Diptangshu Datta Mal[1] | Dongsheng Li[2] | Chuancheng Duan[6] | Hao Li[3] | Peter V. Sushko[2] | Long Luo[1]

[1]Department of Chemistry, University of Utah, Salt Lake City, Utah, USA | [2]Integrated Discovery Sciences Directorate, Pacific Northwest National Laboratory, Richland, Washington, USA | [3]Advanced Institute for Materials Research, Tohoku University, Sendai, Japan | [4]Kummer Institute Center for Resource Sustainability, Missouri University of Science and Technology, Rolla, Missouri, USA | [5]Electron Microscopy and Surface Science Lab, University of Utah, Salt Lake City, Utah, USA | [6]Department of Chemical Engineering, University of Utah, Salt Lake City, Utah, USA

Correspondence: Hao Li (li.hao.b8@tohoku.ac.jp) | Peter V. Sushko (peter.sushko@pnnl.gov) | Long Luo (long.luo@utah.edu)

Received: 16 April 2026 | **Revised:** 21 September 2026 | **Accepted:** 8 October 2026

Keywords: catalytic sensors | grain boundary | humidity tolerance | hydrogen | palladium hydride

ABSTRACT

Reliable hydrogen sensing under high absolute humidity remains a significant challenge owing to the competitive adsorption of water molecules on the sensing material surface. Here, we report a humidity-tolerant catalytic H_2 sensor based on a grain-boundary-rich palladium nanostructure (Pd_{GB}) that operates without any external heating. The Pd_{GB} sensor functions reliably at 22°C–80°C and 0%–90% relative humidity, achieving a lower limit of detection (LLOD) of 100 ppm even at 80°C and 90% relative humidity (261 g m^{-3} absolute humidity, corresponding to a > 3000-fold higher molar concentration of water vapor relative to the LLOD of H_2), while satisfying ISO 26142 requirements for gas sensing. A machine-learning regression model integrated into a sensor prototype enables robust, quantitative determination of H_2 concentration across a wide range of temperature and humidity conditions. Mechanistic investigations combining in situ XRD, temperature-programmed desorption, molecular dynamics simulations, and density functional theory calculations reveal that the exceptional humidity tolerance originates from the Pd grain boundaries, which accelerate PdH_x formation for weakening H_2O adsorption and suppress humidity-induced interference. These findings reveal a previously unexplored synergistic mechanism and establish a general materials-design strategy for next-generation humidity-tolerant catalytic gas sensors.

1 | Introduction

Hydrogen (H_2) serves as a pivotal energy carrier in the global transition toward carbon neutrality. However, the low ignition energy (0.02 mJ) and the wide flammability range (4%–75% in air) pose substantial safety challenges during the production, storage, and transportation of H_2 [1–4]. These challenges are expected to intensify, as the International Energy Agency predicts that global hydrogen demand could increase fivefold over the next 15 years [3]. Such rapid expansion underscores an urgent need for advanced H_2 sensing technologies. Indeed, the global H_2 detection market was valued at USD 224.7 million in 2023 and is projected to grow at approximately 10% annually [5].

Extensive efforts have been devoted over the past decades to developing high-performance gas sensors based on surface

Bingxin Yang, Sampreeti Bhattacharya, and Heng Liu contributed equally to this work.

All rights reserved, including rights for text and data mining and training of artificial intelligence technologies or similar technologies.
© 2026 Wiley-VCH GmbH

acoustic waves [6, 7], electrochemical [8–10], chemiresistive [11–18], chemiFET [19, 20], catalytic [21–23], and optical [24–26] architectures. Among these, catalytic sensors are the most commercially successful, with forecasts predicting an annual market growth rate of 9.5% through 2030 to reach USD 645 million [27], owing to their combination of high sensitivity, selectivity, reproducibility, and accuracy within a compact footprint [28–30]. Catalytic H_2 sensors employ a catalyst, typically a Pt-group catalyst, to promote the exothermic oxidation of hydrogen. The heat generated from this reaction produces a measurable change in the sensor's electrical resistance [29]. Previous studies indicate that these systems offer high sensitivity and LLOD at the ppm level, along with good stability [28–30]. However, existing catalytic H_2 sensors still have not yet achieved ideal performance.

The ISO 26142 standard lists strict performance criteria for stationary H_2 gas sensors [31]. Key requirements include a measurement range often specified by the manufacturer, response times below 30 s, and stable operation at environmental temperatures up to 50°C under 20%–80% relative humidity (RH). Beyond these metrics, sensors should also resist poisoning by hydrocarbons, carbon monoxide, hydrogen sulfide, and other gases, while maintaining power consumption below 1 W [1, 32]. Conventional catalytic H_2 sensors typically require operating temperatures between 200°C and 500°C due to the limited activity of their catalysts [29, 33]. This thermal requirement leads to high power consumption and severe cross-sensitivity to other combustible gases [34]. To address this challenge, our group previously developed a Pt catalyst capable of H_2 oxidation at room temperature without external heating [21]. However, its sensing performance deteriorates significantly under high-humidity conditions.

Although H_2 sensing at high humidity can be achieved using alternative mechanisms at room temperature (Figure 1a), reliable H_2 detection under high humidity at elevated ambient temperatures (T_a > 50°C) remains unmet (see Supplementary Table S1 for the detailed literature survey results). This difficulty arises mainly because the saturation vapor pressure of water increases with temperature; for example, at 80°C and 90% RH, the absolute water vapor concentration is approximately 18 times higher than at 22°C [35]. Several mechanisms may account for the deteriorated performance under high absolute humidity. First, water molecules strongly compete with H_2 for adsorption sites on the sensor surface, thereby suppressing the sensing signal [36]. Reduced accessibility of H_2 to the sensing surface can also hinder sensor recovery [37]. Second, protons generated from the dissociation of adsorbed water may interfere with signal transduction [38]. Achieving simultaneous high humidity tolerance, low power consumption, and selectivity against various interferents therefore remains a long-standing, critical unmet challenge in the field, independent of sensor architecture.

Here, we report a grain-boundary (GB)-rich palladium nanostructure (Pd_{GB}) as a superior catalytic material for humidity-tolerant hydrogen gas sensing. A catalytic sensor constructed with Pd_{GB} enables H_2 detection at T_a values from 22°C to 80°C and RH levels up to 90%, without external heating, thereby ensuring low power consumption. Importantly, the sensor meets the ISO 26142:2010 performance standards even at T_a = 80°C and RH = 80%, while achieving an LLOD of 100 ppm (corresponding to detecting H_2 in the presence of a molar concentration of water vapor > 3000-fold higher). In addition to high sensitivity, this catalytic hydrogen sensor exhibits high selectivity against 21 potential interferents, including CO, CH_4, H_2S, and various volatile organic compounds under dry and high RH conditions. It also maintains stable performance over 100 continuous cycles and 125 days of operation at high absolute humidity. Furthermore, we enabled reliable quantitative prediction of the catalytic H_2 sensing across a broad range of T_a and RH conditions through developing and integrating a Gaussian process regression (GPR) model into a fully functional sensor prototype. Finally, we elucidated the sensing mechanism underlying the high performance of our sensor using in situ XRD experiments, temperature-programmed desorption (TPD), molecular dynamics (MD), and density functional theory (DFT) calculations. The mechanistic study reveals that the Pd_{GB} nanostructure promotes palladium hydride (PdH_x) formation via GB sites even under high humidity. The formed PdH_x phase suppresses H_2O adsorption but actively participates in the catalytic oxidation of H_2.

2 | Results and Discussion

2.1 | Sensing Material Design, Synthesis, and Characterization

Our design of a humidity-tolerant catalytic hydrogen-sensing material, illustrated in Figure 1b, is motivated by several prior findings in the literature. First, DFT calculations from a previous study on Pd-catalyzed H_2O_2 decomposition suggest that water adsorbs more weakly on PdH_x than on metallic Pd as part of a minor step in the proposed reaction pathway [39]. However, this observation was not mechanistically explained in the original work, as it was not central to the study's main conclusions. Second, Pd GBs have been shown to facilitate hydrogen insertion and promote the formation of PdH_x [40]. Third, GBs introduce high-energy surface sites, which often enhance catalytic activity [41]. However, no prior study has leveraged this unexplained DFT observation of weakened H_2O adsorption on PdH_x in combination with the catalytic and hydrogen insertion properties of Pd GBs to engineer humidity tolerance under the simultaneous high-temperature and high-humidity conditions encountered in practical H_2 sensing.

Here, we hypothesize that deliberate engineering of GBs in Pd nanostructures can give rise to a previously unexplored synergistic effect that enhances humidity-tolerant H_2 sensing. Specifically, under high-humidity conditions, hydrogen insertion at GB sites in the presence of H_2 is expected to accelerate PdH_x formation, thereby weakening water adsorption. Concurrently, Pd GBs could possibly promote catalytic activity toward H_2 oxidation in air by facilitating O_2 dissociation like its Pt GB counterparts [21]. To test this hypothesis, we synthesized and systematically characterized Pd materials enriched with GBs (Pd_{GB}). This study aims to provide fundamental insights into hydrogen insertion at Pd GBs in the presence of surface water adsorbates, and to establish a general design strategy for the development of next-generation humidity-tolerant catalytic H_2 sensors.

Pd_{GB} sensing material was synthesized via water-electrolysis-driven assembly of Pd nanoparticles (Pd_{NP}), as previously

15214095, 0, Downloaded from https://advanced.onlinelibrary.wiley.com/doi/10.1002/adma.75476 by Long Luo - University Of Utah J. Willard Marriott Library , Wiley Online Library on [27/10/2026]. See the Terms and Conditions (https://onlinelibrary.wiley.com/terms-and-conditions) on Wiley Online Library for rules of use; OA articles are governed by the applicable Creative Commons License

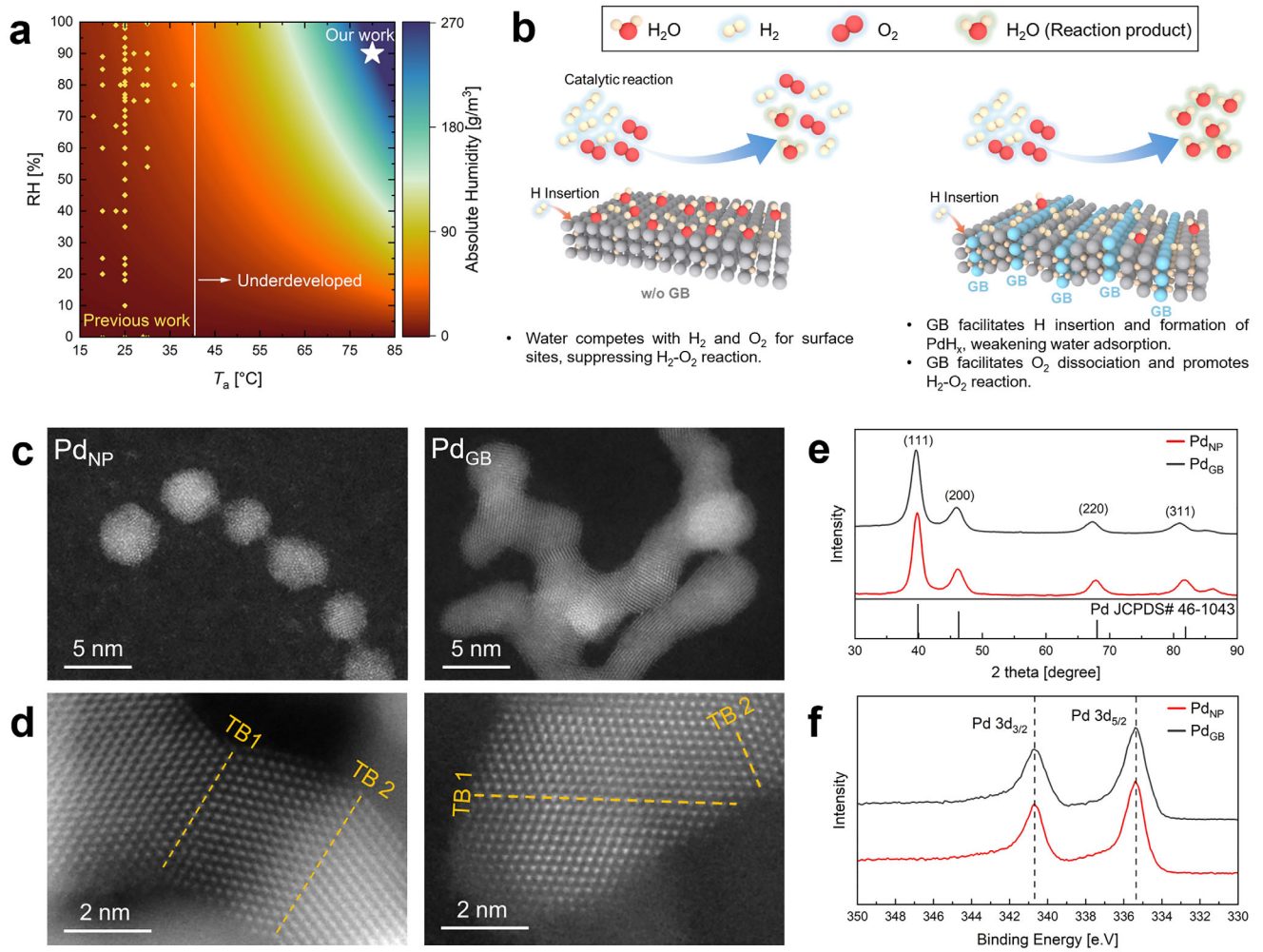


FIGURE 1 | Humidity-tolerant hydrogen sensing material design and structural characterization. (a) Comparison of operational ambient temperature (T_a) and relative humidity (RH) for over 140 state-of-the-art H_2 sensors in the literature (see Table S1) with the sensor reported in this work, where the color map indicates absolute humidity. (b) Proposed sensing material design based on a GB-rich Pd nanostructure (Pd_{GB}), in which blue atoms highlight Pd atoms at GB sites that facilitate hydrogen insertion and catalytic reaction under high humidity, and grey atoms denote Pd atoms at non-GB sites. (c) STEM images of Pd_{NP} and Pd_{GB} showing the interconnected morphology of the Pd_{GB} network. (d) HR-STEM image of Pd_{GB} with Σ3(111) twin boundaries (TB) highlighted by orange dashed lines. (e) XRD patterns confirming the face-centered cubic Pd structure of Pd_{NP} and Pd_{GB}, and (f) XPS spectra of the Pd 3d region for both materials showing characteristic Pd^0 $3d_{5/2}$ and $3d_{3/2}$ peaks.

demonstrated by our group [21, 40]. Scanning transmission electron microscopy (STEM) images (Figure 1c) show that Pd_{GB} forms a densely interconnected network of nanoparticles enriched with GBs. The average crystallite sizes of Pd_{NP} and Pd_{GB} were determined to be 3.6 ± 0.5 nm and 3.9 ± 0.6 nm, respectively, consistent with prior reports [21, 40, 42]. High-resolution STEM (HR-STEM) images of Pd_{GB} (Figure 1d) further reveal that the dominant GBs are Σ3(111) twin boundaries (TBs), highlighted by orange dashed lines. X-ray diffraction (XRD) patterns (Figure 1e) confirm that both Pd_{NP} and Pd_{GB} have the face-centered cubic structure of metallic Pd [14, 43]. X-ray photoelectron spectroscopy (XPS) analysis (Figure 1f and Figure S3) shows only Pd^0 $3d_{5/2}$ and Pd^0 $3d_{3/2}$ peaks at 335.2 and 340.5 eV, respectively, indicating that both materials are fully metallic [44, 45], and the successful removal of surface ligands during the synthesis of Pd_{GB} is supported by the disappearance of C 1s signal from citrate ligands. The mass-specific surface areas of Pd_{GB} and Pd_{NP} were measured to be 20 and 58 $cm^2\ mg^{-1}$, respectively (Figure S4). The lower specific surface area of Pd_{GB} compared with Pd_{NP} results from the loss of exposed surface area associated with nanoparticle attachment during the assembly of Pd_{NP} into Pd_{GB}. The average GB diameter, defined as the diameter of the GB interface formed between two attached Pd NPs (highlighted by the dashed lines in Figure 1d), was measured to be ~3.5 nm. Based on the measured surface area and average GB diameter, the average GB density in Pd_{GB} was estimated to be ~1058 μm^{-1} (see Supporting Information).

2.2 | H_2 Sensing Performance Testing

Catalytic H_2 sensors were fabricated by drop-casting the synthesized Pd_{GB} sensing material onto a thermocouple (Figure S1). The sensing mechanism relies on the catalytic oxidation of H_2 on Pd_{GB} in ambient air, which generates heat and produces a measurable rise in the thermocouple temperature (ΔT), serving as the sensor readout. Figure 2a shows the sensor temperature

15214095, 0, Downloaded from https://advanced.onlinelibrary.wiley.com/doi/10.1002/adma.75476 by Long Luo - University Of Utah J. Willard Marriott Library , Wiley Online Library on [27/10/2026]. See the Terms and Conditions (https://onlinelibrary.wiley.com/terms-and-conditions) on Wiley Online Library for rules of use; OA articles are governed by the applicable Creative Commons License

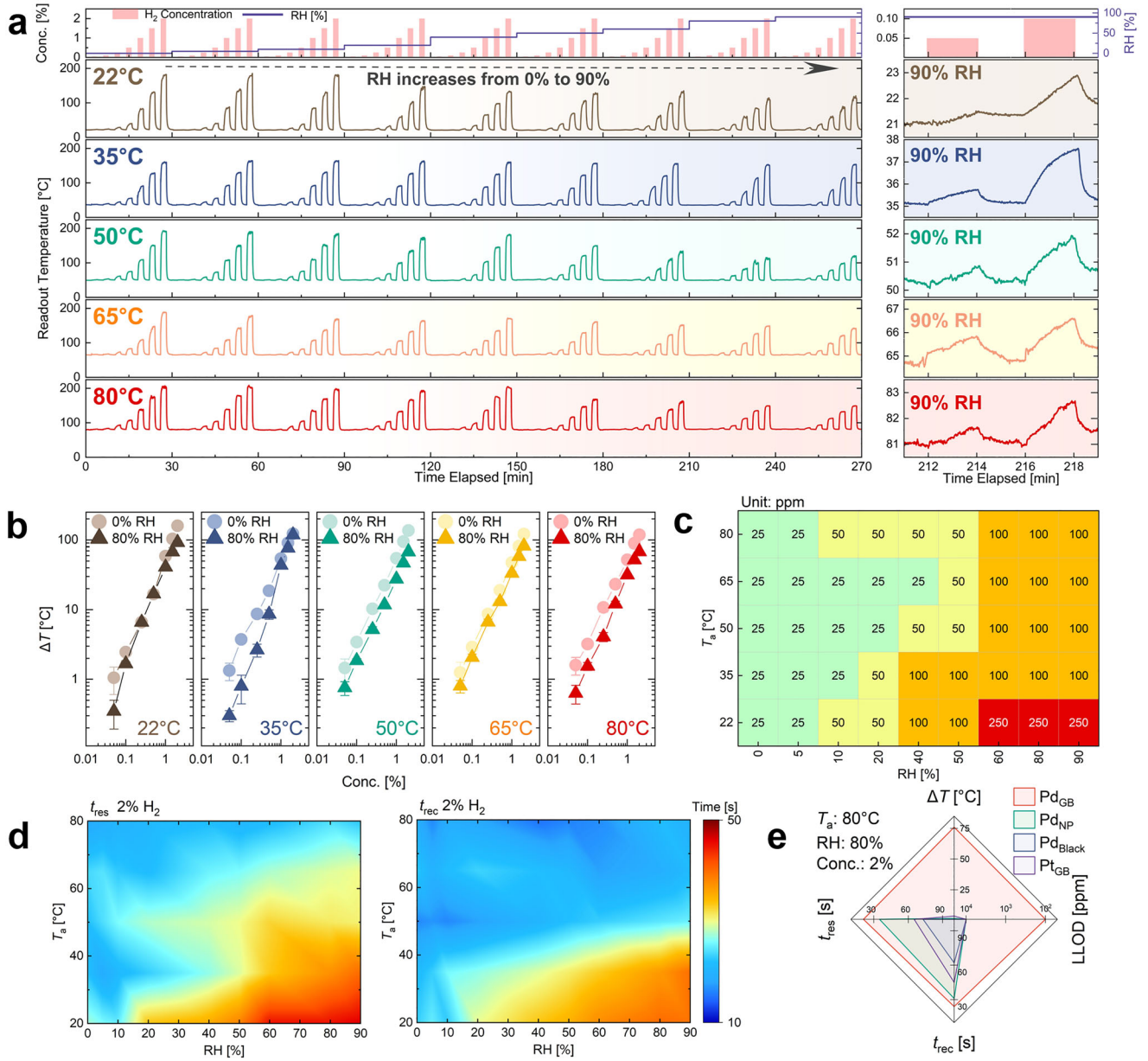


FIGURE 2 | Performance of the Pd_{GB}-based catalytic H_2 sensor under varied ambient temperature and humidity conditions. (a) Sensor temperature change in response to 0.05%–2% H_2 at T_a of 22°C, 35°C, 50°C, 65°C, and 80°C with RH from 0% to 90%, with right panels showing responses to 0.05% and 0.1% H_2 at 90% RH. (b) ΔT as a function of H_2 concentration under 0% and 80% RH across all T_a conditions. (c) Experimentally measured LLOD as a function of T_a and RH. (d) Heat maps of response (t_{res}) and recovery (t_{rec}) times in response to 2% H_2 under various T_a and RH. (e) Comparison of the sensing performance of Pd_{GB}, Pd_{NP}, Pd_{black}, and Pt_{GB} for 2% H_2 in air at 80°C and 80% RH, highlighting the superior sensing performance of Pd_{GB} under high humidity. The error bars in panel b represent the standard deviations from three repeated measurements with the same sensor.

changes in response to various H_2 concentrations (0.05%–2%) at ambient temperature, T_a, of 22°C, 35°C, 50°C, 65°C, and 80°C, with RH increasing from 0% to 90% stepwise every 30 min. Overall, the sensor operates effectively across the full T_a and RH ranges, only exhibiting a slight decrease in response at high temperature and humidity. Figure 2b directly compares the ΔT values at 0% and 80% RH for all five T_a conditions. For example, upon exposure to 2% H_2 at T_a = 22°C, ΔT was 159°C and 91°C under 0% and 80% RH, respectively. At T_a = 80°C, the corresponding responses decreased to 118°C and 68°C. The sensor response is generally linearly correlated with the H_2 concentration at a fixed RH (Figure S8). As highlighted in the right panel of Figure 2a, 0.05% H_2 produces a clearly detectable signal, even at 90% RH. It is worth noting that the molar concentration of water vapor at 80°C and 90% RH is ~14.5 mol/m^3 [35], over 800 times higher than the H_2 concentration in the 0.05% H_2 sample. These observations indicate that, despite adsorbed water molecules partially suppressing catalytic H_2 oxidation on Pd_{GB}, thereby reducing ΔT values, the sensor maintains strong detection capability even under these challenging conditions. For all the tested H_2 concentrations, the steady-state temperature of the catalyst remains at or below the low end of the 200°C–500°C operating range of conventional heated catalytic sensors and far

15214095, 0, Downloaded from https://advanced.onlinelibrary.wiley.com/doi/10.1002/adma.75476 by Long Luo - University Of Utah J. Willard Marriott Library , Wiley Online Library on [27/10/2026]. See the Terms and Conditions (https://onlinelibrary.wiley.com/terms-and-conditions) on Wiley Online Library for rules of use; OA articles are governed by the applicable Creative Commons License

below the ~585°C autoignition temperature of H_2 in air. Therefore, autoignition is not a safety concern under our operating conditions.

The LLOD for the single-thermocouple sensor configuration is constrained by fluctuations in the ambient temperature. To mitigate this effect, we employed a two-thermocouple configuration (Figure S5), in which one thermocouple serves as a reference and the other as the sensing element, enabling a differential signal acquisition that suppresses temperature noise and improves the LLOD. As shown in Figure 2c and Figure S6, the LLOD determined experimentally using the 3σ criterion is as low as 25 ppm when RH < 40% but increases to 250 ppm at T_a = 22°C and RH ≥ 60% with this configuration. Following LLOD determination, we evaluated the dynamic sensing range: the ΔT versus H_2 concentration plots follow a linear dependence on a logarithm-logarithm axis over two orders of magnitude from ~0.01% to 2% (Figure S7).

We further evaluated the response time (t_{res}) and recovery time (t_{rec}), as shown in Figure 2d. For example, upon exposure to 2% H_2 under dry conditions (0% RH), the sensor exhibited a t_{res} of approximately 27 s at T_a = 22°C and 18 s at T_a = 80°C. Upon H_2 removal, the corresponding t_{rec} values were ~23 and ~19 s, respectively. Higher T_a consistently accelerated both response and recovery across all RH conditions. In contrast, elevated humidity slowed them down. At 90% RH, t_{res} increased to ~46 s (22°C) and ~22 s (80°C), while t_{rec} increased to ~40 s (22°C) and ~20 s (80°C). The accelerated response at higher temperatures is attributed to faster adsorption–desorption dynamics and reaction kinetics, as described by the Arrhenius relation. In contrast, the humidity-induced retardation arises from competitive water adsorption on the Pd_{GB} surface.

To benchmark the performance of the Pd_{GB} catalytic H_2 sensor under high humidity conditions, we tested it against sensors prepared using three control Pd catalysts at identical mass loadings: (a) Pd nanoparticles before assembly with surface ligands removed (Pd_{NP}), (b) commercially available Pd black (Pd_{black}), and (c) our previously reported GB-rich Pt nanoparticle assembly (Pt_{GB}) [21]. The performance of all sensors was evaluated at T_a = 80°C and 80% RH (Figure S9). In contrast to Pd_{GB}, the control sensors exhibited markedly smaller ΔT responses (1.8, 0.63, and 3.6°C for Pd_{NP}, Pd_{black}, and Pt_{GB}, respectively) and were unable to detect H_2 concentrations below 1%, which is two orders of magnitude higher than the 100-ppm LLOD achieved with Pd_{GB} (Figure 2e). Pd_{GB} thus outperforms all control catalysts by two orders of magnitude in LLOD under identical harsh conditions. Moreover, both t_{res} and t_{rec} were significantly longer (~ 35 s for Pd_{NP} and ~70 s for Pd_{black} and Pt_{GB}) for the control sensors under 2% H_2 exposure. Together, these results confirm the superior H_2 sensing performance of Pd_{GB} under high-humidity conditions and indicate that its effectiveness stems from its distinctive GB-rich Pd architecture.

We further assessed the operational stability of the Pd_{GB} sensors by subjecting them to 100 consecutive on/off cycles of 2% H_2 at T_a = 22°C (0% RH) and 80°C (80% RH) (Figure 3a). Under both conditions, the ΔT responses remained highly consistent with a relative standard deviation of less than 0.3%, indicating excellent cycling stability. Long-term stability was also evaluated over 125 days under the same two conditions (Figure S12). We observed that the sensor signals only decayed slightly. For instance, at T_a = 80°C and 80% RH, the ΔT response to 2% H_2 decreased by < 9% relative to the original signal (Figure 3b), with a nearly unchanged response to 100–375 ppm H_2 (Figure S13). The impressive stability of our sensor is due to the stable Σ3 GBs in Pd_{GB}, as confirmed by TEM analysis after 4 months (Figure S14).

Additionally, we assessed device-to-device variation on five independently fabricated sensors, using Pd_{GB} catalysts from the same synthesis batch (original, Drop #2, and Drop #3 in Figure 3c) and from different batches (Batch #2 and Batch #3). The sensing test signals nearly perfectly overlapped for all five sensors at T_a = 22°C (0% RH) and at T_a = 80°C (80% RH) (Figure S15 and Figure 3c). Complementary TEM and XRD data (Figures S16 and S17) further substantiated the reproducibility of our sensing material. These results demonstrate that the sensors are highly reproducible, suggesting strong potential for practical deployment. Furthermore, we investigated the effect of the flow rate on the gas-sensing response (Figure S18). The results show that only at flow rates below 750 sccm is the sensor response limited by reactant mass transfer to the catalyst, resulting in a lower response.

In addition to the demonstrated high stability and reproducibility, our sensors exhibit low cross-sensitivity to common interferents and strong tolerance to poisoning. We adopted an established interference/cross-sensitivity testing protocol from the US Department of Energy's National Laboratory of the Rockies with modifications to evaluate both metrics [46]. Using CH_4 as an example, the protocol sequentially exposes the sensor to three on/off cycles of 2% CH_4 in the presence of 2% H_2, followed by three additional on/off cycles of 2% CH_4 (Figure 3d). The sensor readout temperatures upon exposure to 21 different gases at 80°C and 80% RH (as a representative harsh humid condition whose absolute water content is more than ten times that of 22°C at 90% RH)—including CH_4, CO, NO_2, H_2S, and various volatile organic compounds—under both neat and 2% H_2-mixed conditions are shown in Figure 3e and Figure S21. Specifically, when the sensor was exposed to each interfering gas alone, all 21 tested gases produced only minimal changes in ΔT (< 1°C vs. ~70°C in response to 2% H_2 in air). This suggests that, on their own, these gases do not react with O_2 on the catalyst surface at 80°C under 80% RH. When each interfering gas was mixed with 2% H_2, most gases induced less than a 20% deviation from the response obtained with 2% H_2 alone. The increased interference in the presence of H_2 relative to the absence of H_2 is caused by the elevated catalyst temperature due to the H_2 oxidation, which promotes the oxidation of the interfering gases. After removing the interfering gas (Figure S22), the sensor's response to 2% H_2 remained essentially unchanged when comparing the initial measurements with those collected after exposure to all interfering gases in the protocol, indicating excellent resistance to poisoning. The resulting selectivity pattern closely matches that obtained under dry conditions (22°C under 0% RH, Figures S19 and S20), with the interferents alone producing minimal responses and some deviations in the presence of 2% H_2, confirming the low cross-sensitivity and interferent tolerance both at low temperature under dry conditions and at harsh humid conditions.

15214095, 0, Downloaded from https://advanced.onlinelibrary.wiley.com/doi/10.1002/adma.75476 by Long Luo - University Of Utah J. Willard Marriott Library , Wiley Online Library on [27/10/2026]. See the Terms and Conditions (https://onlinelibrary.wiley.com/terms-and-conditions) on Wiley Online Library for rules of use; OA articles are governed by the applicable Creative Commons License

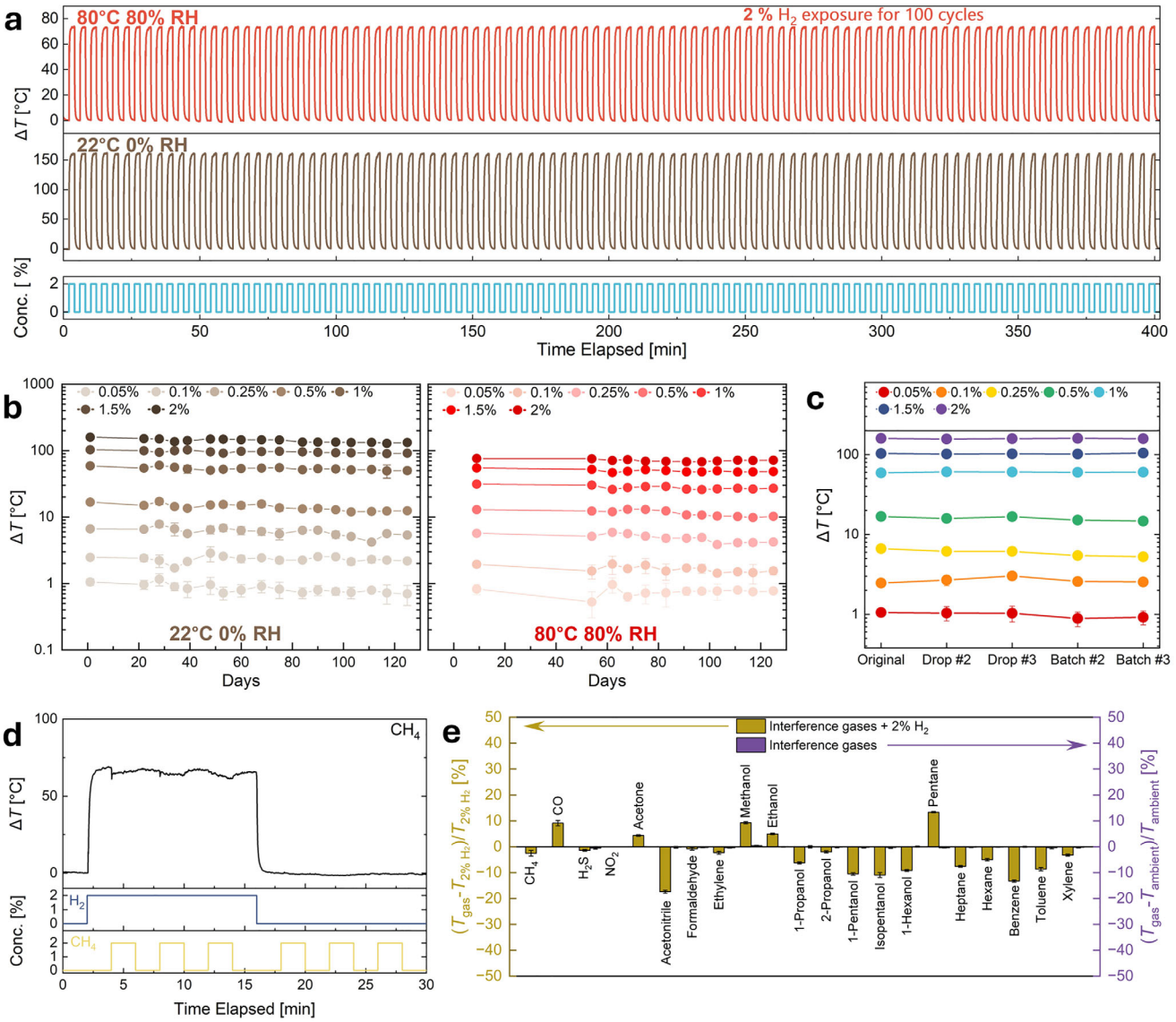


FIGURE 3 | Stability, device-to-device variation, and cross-sensitivity of the catalytic H_2 sensor based on Pd_{GB}. (a) Sensor responses (ΔT) over 100 consecutive on/off cycles of 2% H_2 at $T_a = 22°C$ and 0% RH, and at 80°C and 80% RH. (b) Long-term stability of a sensor stored under ambient conditions for more than 125 days; gas-sensing tests were performed using 0.05%–2% H_2 at $T_a = 22°C$ and 0% RH, and at 80°C and 80% RH. (c) Device-to-device tests were performed on five independently fabricated sensors, using Pd_{GB} catalysts from the same synthesis batch and from different batches. (d) Cross-sensitivity test protocol at 80°C under 80% RH, illustrated using CH_4 as an example: the sensor was sequentially exposed to three on/off cycles of 2% CH_4 in the presence of 2% H_2, followed by three additional on/off cycles of 2% CH_4. (e) Sensor response changes at 80°C under 80% RH in response to a range of interfering gases (CH_4, CO, H_2S, NO_2, and volatile organic compounds) and their mixture with 2% H_2. All interfering gases were tested at 2%, except H_2S (0.2 ppm), NO_2 (2 ppm), and ethylene (2 ppm).

Next, we assessed the robustness of our sensors to humidity variations in accordance with ISO 26142:2010 for H_2 detection. Under this standard, the sensor response at RH values between 20% and 80% must remain within ± 30% of the response measured at 50% RH. This specification defines the allowable window for humidity-induced response variation (Figure 4a, left panel). When the ΔT values obtained at 20%–80% RH were normalized to the value at 50% RH, our sensor satisfied this requirement for 1% H_2 detection at all tested T_a (Figure 4a, right panel). We further evaluated the H_2 response across additional T_a values and at multiple H_2 concentrations (Figure S23). Based on these data, we constructed a 5×7 compliance matrix spanning five T_a settings and seven H_2 concentrations to indicate whether the sensor met the ISO 26142:2010 criterion in each scenario (Figure 4b). The sensor maintained compliance under more than 90% of the tested conditions, surpassing the performance of previously reported H_2 sensors [38].

Finally, we assessed the practical applicability of the Pd_{GB} sensor for detecting H_2 under randomized environmental conditions, which simulate real-world scenarios. We generated 100 random combinations of T_a, RH levels, and H_2 concentration, and tested five independently prepared sensors under these conditions (Figure S24). A representative response trace for 100 randomized conditions is shown in Figure 4c. Because T_a is difficult to control with high temporal precision, we allowed it to drop naturally from

15214095, 0, Downloaded from https://advanced.onlinelibrary.wiley.com/doi/10.1002/adma.75476 by Long Luo - University Of Utah J. Willard Marriott Library , Wiley Online Library on [27/10/2026]. See the Terms and Conditions (https://onlinelibrary.wiley.com/terms-and-conditions) on Wiley Online Library for rules of use; OA articles are governed by the applicable Creative Commons License

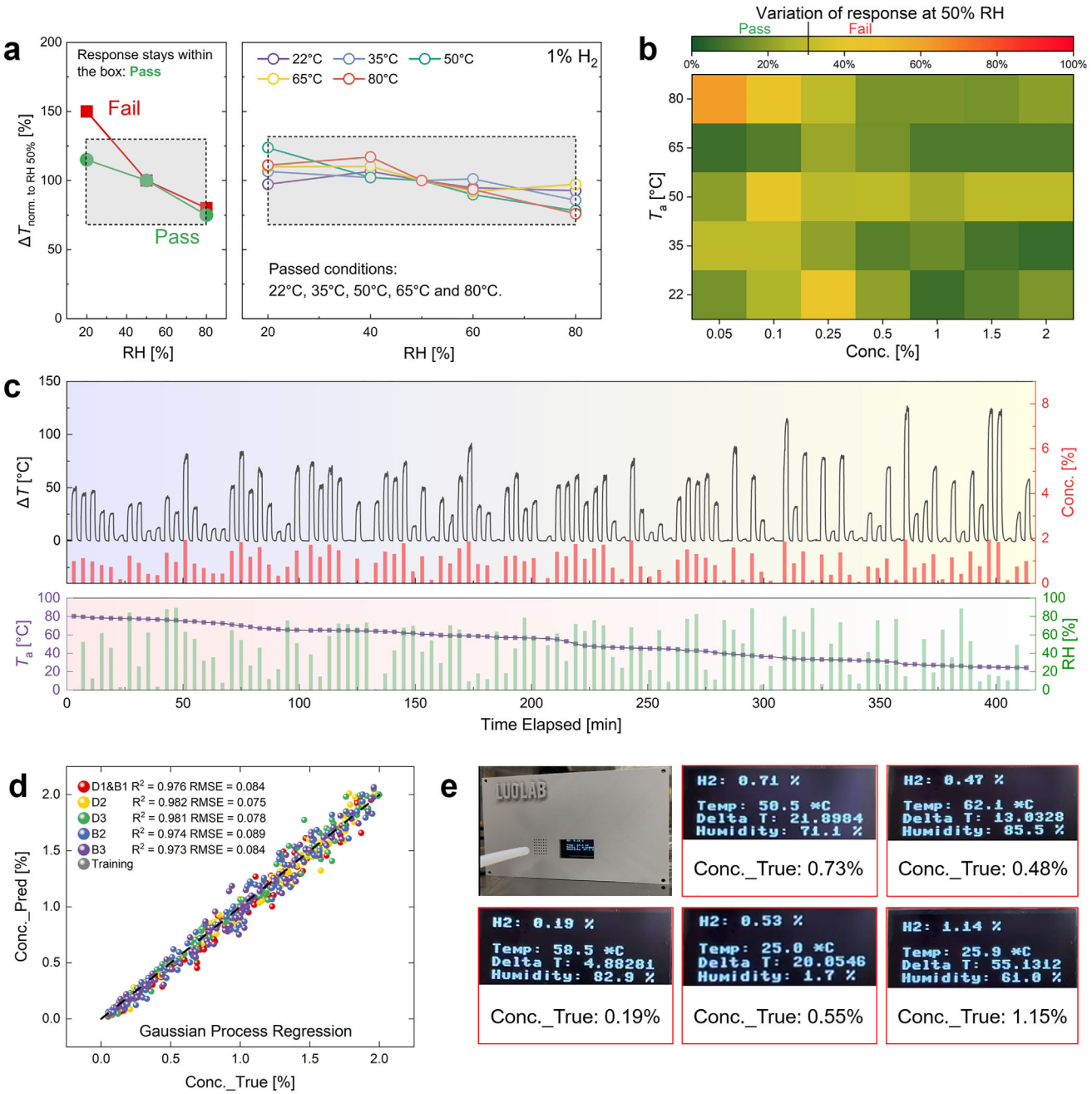


FIGURE 4 | Sensor robustness validation based on ISO 26142:2010 and a machine-learning-algorithm-embedded catalytic H_2 sensor prototype. (a) Illustration of the ISO 26142:2010 requirement and the test result for 1% H_2 sensing. (b) Heatmap of ISO 26142:2010 test results for the Pd_{GB} H_2 sensor under various environmental conditions. (c) Sensing tests under 100 random combinations of T_a, RH levels, and H_2 concentration. T_a drifted naturally from 80°C to room temperature during the measurement sequence. (d) Correlation between predicted and true H_2 concentrations using Gaussian process regression (GPR). RMSE values in the legend are in units of vol% H_2. (e) Real-time measurement of H_2 concentrations across diverse temperature and humidity conditions using the portable sensor prototype with the GPR model embedded.

80°C to room temperature during the measurement sequence. To establish the relationship between H_2 concentration and sensor response under these variable environmental conditions, we evaluated four machine-learning models, namely Gaussian process regression (GPR), support vector regression (SVR), extra trees (ET), and a deep neural network (DNN) (Figure S25). Among them, the GPR model displayed the best predictive performance, as evidenced by the close agreement between measured and predicted H_2 concentrations (Figure 4d). Test datasets collected from all five sensors closely follow the 1:1 reference line with R^2 values of 0.973–0.982 and RMSE values of 0.075–0.089, indicating that the model generalizes well across different synthesis batches and operating conditions. Based on these results, we developed a simple prototype H_2 sensor incorporating the GPR model (Figure 4e and Figure S2). When evaluated under randomized combinations of H_2 concentration, RH, and T_a, the predicted H_2 concentrations agreed with the actual values to within 5%. These findings demonstrate that the

15214095, 0, Downloaded from https://advanced.onlinelibrary.wiley.com/doi/10.1002/adma.75476 by Long Luo - University Of Utah J. Willard Marriott Library , Wiley Online Library on [27/10/2026]. See the Terms and Conditions (https://onlinelibrary.wiley.com/terms-and-conditions) on Wiley Online Library for rules of use; OA articles are governed by the applicable Creative Commons License

machine-learning-algorithm-embedded Pd_{GB} sensor provides robust and reliable quantitative H_2 measurements, highlighting its strong potential for practical deployment.

2.3 | Humidity-Tolerant Catalytic Sensing Mechanism

To elucidate the mechanism underlying the Pd_{GB} sensor's high-humidity tolerance and understand the role of Pd GBs, we first verified that GB sites are responsible for the enhanced H_2 sensing activity. We synthesized Pd_{GB} materials with varying GB densities and correlated the GB density of the NP assembly with its H_2-sensing performance. Specifically, we synthesized Pd_{GB} samples with different GB densities by tuning the electrogelation potential from 1.5 to 4.0 V (Figure S10). This modulation is feasible because at higher potentials, more rapid bubble generation induces stronger local flow, which promotes interparticle connectivity and consequently leads to a higher GB density [21]. We electrochemically measured that the GB density of the Pd nanoparticle assembly increased from ~700 μm^{-1} at −1.5 V to ~1800 μm^{-1} at −4.0 V (Figure S11). Using these materials with systematically varied GB densities, we evaluated their H_2 sensing performance at $T_a = 22°C$ under dry conditions and at $T_a = 80°C$ under 80% RH (Figure S11). The results show a clear positive correlation between GB density and ΔT response, suggesting that a higher GB density leads to enhanced catalytic activity and improved H_2 sensitivity.

Next, we performed in situ XRD measurements to test the hypothesis that Pd GBs facilitate rapid PdH_x formation even under high-humidity conditions. Figure 5 shows the Pd (111) XRD peak for Pd_{NP} without surface ligands (Figure 5a) and for Pd_{GB} (Figure 5b) upon exposure to 2% H_2 in N_2 at RH = 0% (left) and 100% (right). The (111) peak intensity transition of Pd under these conditions is summarized in Figure S27. N_2-balanced H_2 was used to avoid complications arising from O_2 adsorption on the catalytic surface and the exothermic H_2−O_2 reaction. The shift of the Pd (111) peak from ~39.5° to ~39.2° in 2θ corresponds to the transformation of Pd into PdH_x upon H_2 exposure. Notably, PdH_x formed more rapidly in Pd_{GB} (~6 s) than in Pd_{NP} (~27 s) at RH = 0%, consistent with our previous findings [40]. Strikingly, as the RH increased from 0% to 100%, the PdH_x formation time in Pd_{GB} extended to ~12 s modestly. In contrast, PdH_x formation in Pd_{NP} was nearly completely inhibited with no XRD peak shift in ~1 min and an incomplete shift even after 10 min (Figure S28). These results indicate that (1) water vapor strongly competes with H_2 for adsorption on Pd surfaces, thereby hindering H_2 dissociation and diffusion, and (2) Pd GBs provide an alternative, more accessible pathway for hydrogen insertion, enabling PdH_x formation even under high-humidity conditions.

To understand how Pd GBs enable efficient H trapping and insertion under high-humidity conditions, we first examined the interaction of a thin H_2O layer with a corrugated Pd surface using an MD model, where the concave and convex topographic features are associated with Σ3(111) GBs (Figure 5c and Figure S32). To mimic high-humidity conditions, we considered 1.125 monolayer (ML) H_2O coverage, assuming that 1 ML corresponds to the continuous H_2O hexamer network distorted by the concave and convex features. The MD simulations performed using the constant number of particles (N), volume (V), and temperature (T) or NVT ensemble at T = 300 K, demonstrate that oxygen atoms of the adsorbed H_2O monolayer primarily reside above the surface Pd atoms, as expected, and that excess H_2O is unstructured (Figures S30 and S31). In addition, O-atom locations near the concave sites of Σ3(111) GBs are smeared away from the surface Pd atoms (Position 3 in Figure 5d), which reflects enhanced dynamics in this region. We attribute this enhancement to competition between binding environments formed by the intersection of two Pd (111) planes and to strain imposed on the hexamer network. As a result, the Pd–O distance at the concave site is larger than that at the (111) terraces and near the convex sites (Figure S30).

To account for the possibility of forming multiple H_2O layers under high humidity conditions, we also performed MD simulations using the same Pd surface model as above but initially covered by two monolayers of H_2O. The results show that water molecules in the second water layer tend to aggregate, whereas the first water layer remains relatively immobile on the Pd surface (Figure S33). This aggregation becomes more pronounced as the temperature increases, leading to the formation of nanoscale water droplets (Figure S34). Overall, these results suggest that the Pd GB surface is likely covered by a combination of a monolayer of water in some regions and multilayer water clusters in others. We expect H_2 to penetrate through regions covered by a water monolayer to interact with the Pd surface, rather than through regions covered by thicker water layers. Therefore, the conclusion from the monolayer simulations discussed above should hold even when multiple layers of water could be present.

We then computationally evaluated possible pathways for H_2 to penetrate the monolayer of adsorbed water and reach Pd GB sites as H atoms for PdH_x formation. Two pathways were considered, as illustrated in Figure 5e and Figures S35 and S36. In Pathway I, H_2 directly diffuses through the H_2O monolayer to the Pd surface and then dissociates into two adsorbed H atoms. These diffusion and dissociation processes proceed with negligible barriers given the differences in sizes of the H_2 molecule and the hexamer ring (0.75 and ~5 Å, respectively) and the well-established ability of Pd to dissociate H_2. In Pathway II, H_2 diffuses through the H_2O layer and dissociates into an adsorbed H atom, an H^+ bound to an H_2O molecule to form H_3O^+, and an electron transferred to Pd. Thermodynamically, both pathways are feasible, but the water-assisted Pathway II is ~0.18 eV more favorable than Pathway I; in addition, it preferentially takes place near concave sites where H_3O^+ is the most stable (see Figure S36). Once H reaches the Pd GB sites, further insertion into bulk Pd along the GB is energetically more favorable than insertion at sites away from the GB, according to our recent findings [40]. This process ultimately leads to the formation of the PdH_x phase.

To study the impact of PdH_x formation on the H_2O adsorption behavior on Pd_{NP} and Pd_{GB}, we performed temperature-programmed desorption (TPD) experiments under both H_2O-only and H_2O + H_2 conditions (Figure 6a and Figure S29). For Pd_{NP}, the H_2O-only trace (purple curve in the top panel) returned to baseline at ~175°C. Upon introducing H_2, the baseline was restored slightly earlier at ~170°C, indicating only a modest reduction in net H_2O adsorption, consistent with limited PdH_x formation observed in the in situ XRD experiment. In

15214095, 0, Downloaded from https://advanced.onlinelibrary.wiley.com/doi/10.1002/adma.75476 by Long Luo - University Of Utah J. Willard Marriott Library , Wiley Online Library on [27/10/2026]. See the Terms and Conditions (https://onlinelibrary.wiley.com/terms-and-conditions) on Wiley Online Library for rules of use; OA articles are governed by the applicable Creative Commons License

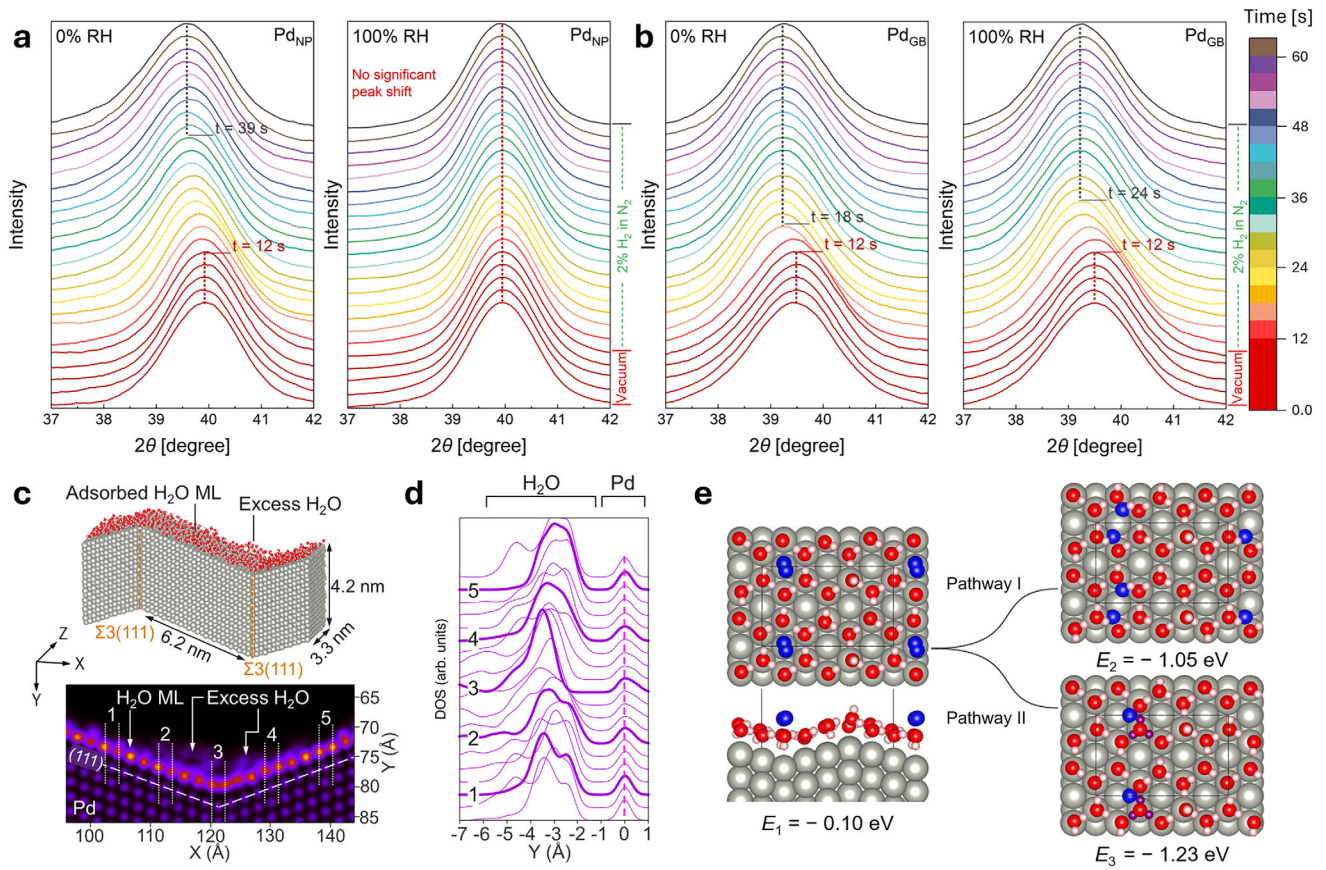


FIGURE 5 | Humidity-tolerant catalytic H_2 sensing mechanism. (a, b) Time-resolved Pd (111) XRD peak shifts for (a) Pd_{NP} and (b) Pd_{GB} upon exposure to 2% H_2 (N_2 balanced) under 0% RH and 100% RH. (c) Top: MD modeling of the interaction between 1.125 ML of H_2O and a corrugated Pd surface, where concave and convex topographic features correspond to Σ3(111) GBs. Gray spheres represent Pd atoms, red spheres O atoms, and white spheres H atoms. Bottom: Heat map representation of the calculated spatial density of H_2O molecules on the Pd surface. (d) Distribution of the density of states (DOS) of H_2O molecules on the Pd surface as a function of distance from the center of the surface Pd atom at 0 Å. (e) DFT-calculated adsorption energies for H_2 (blue) bound to a water monolayer (left) and as products of dissociative interaction with Pd_{GB} in high-humidity conditions. Pathway I: direct H_2 diffusion through the H_2O layer to the Pd surface, followed by H_2 dissociation into two adsorbed H atoms, and pathway II: H_2 dissociation in the vicinity of the Pd surface into an adsorbed H atom, a H^+ bound to an H_2O molecule forming H_3O^+ (H atoms are shown in purple), and e^- transferred into Pd. Black rectangles indicate boundaries of the periodic supercell.

comparison, Pd_{GB} exhibited a similar H_2O desorption profile under H_2O-only conditions, with baseline recovery slightly delayed to ~180°C. However, under H_2O + H_2 conditions, Pd_{GB} recovered much earlier, with the baseline restored at ~140°C. Quantitatively, the integrated signal fraction decreased by ~50% for Pd_{GB}, markedly larger than that for Pd_{NP} (~11%). These results indicate that H_2 more effectively suppresses H_2O adsorption on Pd_{GB} than on Pd_{NP}, possibly because Pd_{GB} promotes PdH_x formation, which weakens H_2O adsorption.

We validated the weakening effect of PdH_x formation on H_2O adsorption by calculating and comparing the adsorption energies of H_2O on the Pd_{GB} and PdH_{GB} models. According to the in situ XRD results, bulk-phase PdH_x forms when the Pd_{GB} catalyst is exposed to an H_2 concentration of ~2% at 100% RH; therefore, we used a fully hydrided Pd structure to represent the PdH_{GB} model (Figure 6b). The calculations show that H_2O adsorption on Pd_{GB} is exothermic, with an adsorption energy of −0.24 eV. In contrast, H_2O does not adsorb on PdH_{GB} due to a positive adsorption energy of 0.18 eV, indicating that PdH_x formation significantly weakens H_2O adsorption, consistent with the TPD results. This finding is also consistent with a previous study, which showed that GBs at concave sites facilitate PdH_x formation, thereby weakening the adsorption of other species [42]. O_2 adsorption, however, remains favorable on both surfaces, with adsorption energies of −1.25 eV on Pd_{GB} and −0.77 eV on PdH_{GB}. Thus, O_2 binds approximately 1 eV more strongly than H_2O on both surfaces, allowing O_2 to outcompete H_2O for adsorption at the GB sites.

The next question is: how does PdH_x formation influence catalytic hydrogen oxidation? We addressed this question by experimentally evaluating the reactivity of PdH_x with O_2 (Figure 6c). We first exposed Pd_{GB} to 2% H_2 in Ar, which produced an initial temperature rise of ~2°C over ~10 s before reaching a steady state. This initial increase corresponds to the exothermic insertion of hydrogen into Pd to form PdH_x (the standard enthalpy of formation for bulk PdH_x is ~ −33 kJ mol^{-1} H_2) [47]. We then rapidly switched the gas flow from H_2/Ar to O_2 and observed an immediate temperature jump followed by a gradual decay over ~100 s. Because the gas-switching process completes within a few seconds, the observed temperature rise is attributed primarily to the reaction of PdH_x with O_2 rather than to direct H_2–O_2

15214095, 0, Downloaded from https://advanced.onlinelibrary.wiley.com/doi/10.1002/adma.75476 by Long Luo - University Of Utah J. Willard Marriott Library , Wiley Online Library on [27/10/2026]. See the Terms and Conditions (https://onlinelibrary.wiley.com/terms-and-conditions) on Wiley Online Library for rules of use; OA articles are governed by the applicable Creative Commons License

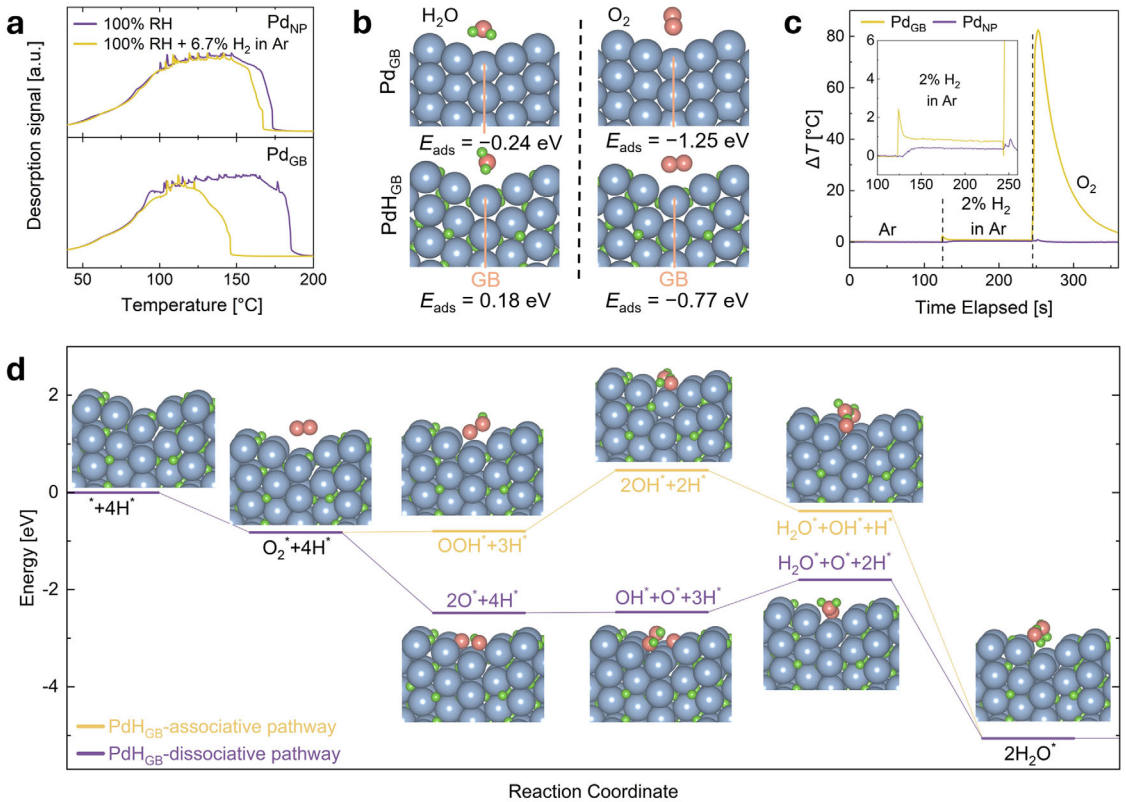


FIGURE 6 | Catalytic H_2 sensing mechanism. (a) TPD profiles collected under 100% RH (purple) and under 100% RH with 6.7% H_2 in Ar (yellow) for Pd_{NP} (top panel) and Pd_{GB} (bottom panel), showing the effect of H_2 on the H_2O desorption behavior. (b) Optimized adsorption configurations and calculated adsorption energies of H_2O (left panel) and O_2 (right panel) on Pd_{GB} (top panel) and PdH_{GB} (bottom panel). (c) Temperature changes of Pd_{NP} and Pd_{GB} catalysts during sequential exposure to Ar, 2% H_2 in Ar, and O_2. (d) Free energy diagrams of the associative and dissociative H_2 oxidation pathways on PdH_{GB}. Insets show the optimized configurations of each intermediate state. Color coding: blue represents Pd, red represents O, and green represents H.

oxidation. This result demonstrates that PdH_x is highly reactive toward O_2 and plays a central role in the catalytic oxidation pathway. Next, we compared the associative and dissociative pathways for O_2–PdH_x reaction using the fully hydrided Pd structure (i.e., PdH_{GB} model) using DFT calculations (Figure 6d). In the associative pathway, adsorbed O_2 is first hydrogenated to OOH*, followed by O–O bond cleavage. In the dissociative pathway, O_2* first dissociates into two O* species, which are subsequently hydrogenated stepwise to OH* and H_2O*. The largest uphill reaction-energy change along the dissociative pathway is 0.67 eV, substantially lower than the corresponding value of 1.26 eV along the associative pathway. These reaction-energy profiles suggest that the dissociative pathway is thermodynamically more favorable on PdH_x, with dissociated O* consuming surface hydrogen supplied by PdH_x to form water. We note that this mechanism applies to the high-H_2-concentration regime, in which O_2 reacts with PdH_x to release heat.

Altogether, we think that the high-humidity tolerance of the Pd_{GB} sensor originates from its unique GB structure, which disrupts the adsorbed H_2O network at the GB sites and enables the rapid Pd-to-PdH_x transition in the presence of H_2 under high-humidity conditions. The formation of PdH_x weakens H_2O adsorption, thereby further reducing the surface coverage of H_2O and promoting the exothermic reaction between PdH_x and O_2. The resulting self-heating of the catalyst can further decrease H_2O surface coverage and accelerate the reaction between H_2 and O_2. At low H_2 concentrations, such as 100 ppm, however, the measured increase in catalyst temperature is small (< 1.5°C), while the sensor still performs well over a wide humidity range of 0%–90% RH. This indicates that the facilitated PdH_x formation should be the major contributor to the humidity tolerance, at least under low-H_2-concentration conditions.

We also want to point out that the Pd_{GB} sensor exhibits high H_2 sensing performance at low RH, where H_2O adsorption is not a significant issue. The DFT results in Figures S37 and S38 show that O_2 readily dissociates at the GB sites with a very low activation barrier of only 0.05 eV. This enables a dissociative H_2–O_2 reaction pathway at the Pd GB sites with an activation barrier of 0.34 eV, which is lower than the 0.45 eV barrier for the associative pathway on the pristine Pd(111) surface. These results indicate that the intrinsically high catalytic activity of the GB sites also contributes to the excellent H_2 sensing performance of the Pd_{GB} sensor.

3 | Conclusion

In conclusion, we have demonstrated that grain-boundary-rich palladium nanostructures (Pd_{GB}) provide a powerful platform for humidity-tolerant, low-power catalytic hydrogen sensing. The

15214095, 0, Downloaded from https://advanced.onlinelibrary.wiley.com/doi/10.1002/adma.75476 by Long Luo - University Of Utah J. Willard Marriott Library , Wiley Online Library on [27/10/2026]. See the Terms and Conditions (https://onlinelibrary.wiley.com/terms-and-conditions) on Wiley Online Library for rules of use; OA articles are governed by the applicable Creative Commons License

Pd_{GB} sensor achieves reliable quantitative detection from 22°C to 80°C and up to 90% RH, maintains a 100-ppm LLOD under extreme absolute humidity, and meets ISO 26142 requirements while exhibiting excellent stability over 125 days, reproducibility, and selectivity against more than 20 interferents. In situ XRD and MD simulations reveal that Σ3(111) GBs retain their ability to facilitate rapid PdH_x formation even under high-humidity conditions and to activate O_2. Meanwhile, TPD experiments suggest that the extensive formation of PdH_x on Pd_{GB} upon H_2 exposure significantly promotes the H_2O desorption. In the catalytic hydrogen oxidation, the formed PdH_x is demonstrated to be reactive toward O_2 and plays a central role in the catalytic oxidation pathway. These results provide fundamental insight and strong support for mitigating competitive H_2O adsorption and for robust sensing performance under challenging environmental conditions. In addition, integrated with a Gaussian process regression model, the sensor further delivers accurate real-time H_2 quantification across dynamically varying conditions. By revealing a previously unexplored synergistic mechanism and establishing a general defect-engineering strategy, this work paves the way for next-generation catalytic gas sensors capable of reliable operation under extreme real-world conditions.

4 | Experimental Section

Synthesis of Pd_{NP_ligand} was performed according to our previously reported protocol with minor modifications [21]. In general, 0.14 mmol potassium tetrachloropalladate(II) (K_2PdCl_4, 98%, Sigma-Aldrich), 0.07 mmol sodium citrate tribasic dihydrate (NaCA) ($C_6H_5Na_3O_7{\cdot}2H_2O$, ≥ 99%, Sigma-Aldrich), and 0.3 mmol sodium borohydride ($NaBH_4$, ≥ 98%, MP Biomedicals) were predissolved in 20, 10, and 5 mL of deionized water (DI H_2O, PURELAB, 18.2 MΩ cm, total organic carbon < 3 ppb), respectively. Subsequently, 20 mL of an aqueous solution of 0.14 mmol K_2PdCl_4 was then added to 400 mL of DI H_2O for 1 min under vigorous stirring without heating, followed by 10 mL of an aqueous solution of NaCA for another 1 min. Finally, the 5 mL aqueous solution of 0.3 mmol $NaBH_4$ was gradually dropped into the solution and reacted for 30 min.

Pd_{GB} was synthesized via an electrogelation process previously reported [21]. The as-obtained Pd_{NP_ligand} solution was first concentrated via the rotary evaporator to 125 mL. Before the electrogelation process, the working electrode (Pt foil, ~240 mm^2) and counter electrode (Pt foil, ~385 mm^2) were polished electrochemically in 0.5 M H_2SO_4 aqueous solution for 500 cycles between 1.1 and −0.23 V with a sweep rate of 0.1 V/s (CHI 650E, CH Instruments), using an Ag/AgCl/saturated KCl electrode as a reference. After electrode cleaning, 8 mL of concentrated Pd_{NP_ligand} solution was used to prepare Pd_{GB}. A potential of −2 V was applied on the working electrode for several hours until the Pd_{GB} precipitated at the bottom of the beaker and Pd_{NP_ligand} solution supernatant became transparent. This phenomenon indicated a successful assembly of Pd_{NP_ligand} to wet Pd_{GB}. Subsequently, Pd_{GB} was meticulously collected from the bottom and transferred into a glass vial, then washed with DI H_2O 10 times over approximately a week. For each washing cycle, the suspension was left undisturbed until the Pd-based materials completely precipitated to the bottom of the vial and the supernatant became clear. The supernatant was then carefully removed, and fresh DI H_2O was added to redisperse the precipitate for subsequent washing. Thereafter, the Critical Point Drying (CPD, EM CPD300, Leica) was adopted for wet Pd_{GB} drying. Before the CPD process, the solvent in wet Pd_{GB} was exchanged with acetone (C_3H_6O, ≥ 99.5%, Sigma-Aldrich) by removing the supernatant and refilling with fresh acetone ten times. After solvent exchange, the wet Pd_{GB} in acetone was subjected to supercritical drying, and dry Pd_{GB} was obtained after approximately 45 min. The dry Pd_{GB} was then dispersed in a mixture of DI H_2O and acetone (1:1, *v*/*v*) to obtain a slurry (Pd_{GB} slurry) with a concentration of 10 mg/mL for future use.

The gas sensors were fabricated by drop casting the proper amount of catalyst slurries onto a J-type thermocouple, and the sensing performance was evaluated using a custom gas sensor testing system (Figure S1). The sensor response (ΔT) was defined as the temperature difference between the final one-second readout and the initial sensor readout for each concentration test. The response time (t_{res}) was defined as the time required for the sensor signal to reach 90% of its steady-state temperature after exposure to the H_2 gas, while the recovery time (t_{rec}) corresponded to the time needed for the signal to return to 90% of the temperature baseline value once the H_2 gas was removed. Unless otherwise noted, error bars represent the standard deviation of three repeated measurements on the same sensor.

Additional experimental details, including the synthesis of the other catalysts, sensing materials preparation, sensor fabrication, sensor testing protocols, and theoretical calculation methods, are provided in the Supporting Information.

Author Contributions

Bingxin Yang: conceptualization, methodology, visualization, writing – original draft, writing – review and editing, validation, investigation, formal analysis, data curation. **Sampreeti Bhattacharya**: conceptualization, methodology, investigation, validation, writing – original draft, writing – review and editing, software, data curation, visualization. **Heng Liu**: conceptualization, methodology, data curation, formal analysis, validation, investigation, visualization, writing – original draft, writing – review and editing. **Michael A. Pence**: methodology, data curation, formal analysis, visualization, writing – original draft. **K. A. U. Madhushani**: methodology, data curation, formal analysis. **Bobby G. Duersch**: methodology, data curation, formal analysis. **Linfeng Yu**: methodology, data curation, formal analysis. **Hyoju Park**: methodology, formal analysis, data curation. **Diptangshu Datta Mal**: methodology, formal analysis, data curation. **Dongsheng Li**: methodology, formal analysis, data curation, supervision. **Chuancheng Duan**: supervision, formal analysis, resources, project administration, methodology, funding acquisition. **Hao Li**: methodology, project administration, resources, supervision, formal analysis, funding acquisition, writing – original draft, writing – review and editing. **Peter V. Sushko**: methodology, formal analysis, supervision, data curation, resources, project administration, visualization, investigation, validation, funding acquisition, writing – original draft, writing – review and editing. **Long Luo**: conceptualization, methodology, data curation, supervision, formal analysis, funding acquisition, visualization, project administration, resources, writing – review and editing, writing – original draft, investigation, validation.

Acknowledgements

This research was supported by the US Department of Energy (DOE), Office of Science (SC), Office of Basic Energy Sciences (BES), Materials

15214095, 0, Downloaded from https://advanced.onlinelibrary.wiley.com/doi/10.1002/adma.75476 by Long Luo - University Of Utah J. Willard Marriott Library , Wiley Online Library on [27/10/2026]. See the Terms and Conditions (https://onlinelibrary.wiley.com/terms-and-conditions) on Wiley Online Library for rules of use; OA articles are governed by the applicable Creative Commons License

Sciences and Engineering Division, Synthesis and Processing Science Program, FWP 78705. Long Luo also gratefully acknowledges support from the University of Utah and the Alfred P. Sloan Foundation (Grant Number FH-2023-20829) for supporting the lab setup. Mike Pence was supported by the National Science Foundation MPS-Ascend Postdoctoral Research Fellowship under Grant Number. CHE-2503457. TEM was conducted in the William R. Wiley Environmental Molecular Sciences Laboratory (EMSL), a national scientific user facility sponsored by the DOE Office of Biological and Environmental Research located at PNNL. This research used resources of the National Energy Research Scientific Computing Center, a DOE SC User Facility supported by the SC of the US DOE under Contract No. DE-AC02-05CH11231 using NERSC award BES-ERCAP0037225. This work made use of Nanofab EMSAL shared facilities of the Micron Technology Foundation Inc. Microscopy Suite sponsored by the John and Marcia Price College of Engineering, Health Sciences Center, Office of the Vice President for Research, and by the MRSEC Program of the NSF under Award No. DMR-112125. Acquisition of the Bruker D8 Discover system was made possible by the Air Force Office of Scientific Research under project number FA9550-21-1-0293. TPD was conducted by Linfeng Yu and Chuancheng Duan, supported by the Army Research Office under Cooperative Agreement Numbers W911NF2410391 and W911NF-23-C-0038. We also thank Dr. Miao Xu at Honeywell for the helpful discussion and feedback. ChatGPT was used to improve the language and clarity of the manuscript during its preparation.

Funding

This research was supported by the US Department of Energy (DOE), Office of Science (SC), Office of Basic Energy Sciences (BES), Materials Sciences and Engineering Division, Synthesis and Processing Science Program, FWP 78705. Long Luo also gratefully acknowledges support from the University of Utah and the Alfred P. Sloan Foundation (Grant # FH-2023-20829) for supporting the lab setup. Mike Pence was supported by the National Science Foundation MPS-Ascend Postdoctoral Research Fellowship under Grant No. CHE-2503457. TEM was conducted in the William R. Wiley Environmental Molecular Sciences Laboratory (EMSL), a national scientific user facility sponsored by the DOE Office of Biological and Environmental Research located at PNNL. This research used resources of the National Energy Research Scientific Computing Center, a DOE SC User Facility supported by the SC of the U.S. DOE under Contract No. DE-AC02-05CH11231 using NERSC award BES-ERCAP0037225. This work made use of Nanofab EMSAL shared facilities of the Micron Technology Foundation Inc. Microscopy Suite sponsored by the John and Marcia Price College of Engineering, Health Sciences Center, Office of the Vice President for Research, and by the MRSEC Program of the NSF under Award No. DMR-112125. Acquisition of the Bruker D8 Discover system was made possible by the Air Force Office of Scientific Research under project number FA9550-21-1-0293. TPD was conducted by Linfeng Yu and Chuancheng Duan, supported by the Army Research Office under Cooperative Agreement Numbers W911NF2410391 and W911NF-23-C-0038.

Conflicts of Interest

A US provisional patent application (no. 63/930,226) based on the technology described in this work was filed on December third, 2025, by Long Luo and Bingxin Yang at the University of Utah.

Data Availability Statement

The data that supports the findings of this study are available in the supplementary material of this article.

References

1. I. Darmadi, F. A. A. Nugroho, and C. Langhammer, "High-Performance Nanostructured Palladium-Based Hydrogen Sensors—Current Limitations and Strategies for Their Mitigation," *ACS Sensors* 5 (2020): 3306.

2. W.-T. Koo, H.-J. Cho, D.-H. Kim, et al., "Chemiresistive Hydrogen Sensors: Fundamentals, Recent Advances, and Challenges," *ACS Nano* 14 (2020): 14284–14322, https://doi.org/10.1021/acsnano.0c05307.

3. T. M. Swager, T. N. Pioch, H. Feng, H. M. Bergman, S.-X. L. Luo, and J. J. I. Valenza, "Critical Sensing Modalities for Hydrogen: Technical Needs and Status of the Field to Support a Changing Energy Landscape," *ACS Sensors* 9 (2024): 2205.

4. J. Zhu, Y. Zhan, X. Ni, and Y. Gao, "Artificial Intelligence of Things in Hydrogen Sensing: Toward Optic and Intelligent System," *Research* 8 (2025): 0750, https://doi.org/10.34133/research.0750.

5. S. Gujar and T. Malwa, Hydrogen Detection Market Size, Share & Growth Report – 2032, Global Market Insights, Inc., 2024, https://www.gminsights.com/industry-analysis/hydrogen-detection-market.

6. J. Jin, B. Cui, L. Zhou, et al., "Influence of the Pd Oxidation State in PdNi Thin Films on Surface Acoustic Wave Hydrogen Sensing Performance," *ACS Sensors* 9 (2024): 2395.

7. X. Wang, L. Du, L. Cheng, et al., "Pd/Ni Nanowire Film Coated SAW Hydrogen Sensor With Fast Response," *Sensors and Actuators B: Chemical* 351 (2022): 130952, https://doi.org/10.1016/j.snb.2021.130952.

8. L. Huang, H. Sun, W. Li, et al., "Pt Loading of Phosphorus-Doped Carbon Nanotube Aerogels in Fuel Cell-Type Gas Sensors for Ultrasensitive H_2 Detection," *ACS Sensors* 9 (2024): 3763.

9. L. Wang and J. Yi, "Tailoring the Electrochemical Activities of Doped Ceria by Tuning Acidity for Boosted H_2 Sensing," *Sensors and Actuators B: Chemical* 398 (2024): 134723, https://doi.org/10.1016/j.snb.2023.134723.

10. H. Zhang, L. Huang, Y. Li, Y. Liu, X. Liang, and G. Lu, "Development of a Miniaturized Current Type H_2 Gas Sensor Based on Nafion and Pt-Pd/C Sensing Electrode," *Sensors and Actuators B: Chemical* 430 (2025): 137366, https://doi.org/10.1016/j.snb.2025.137366.

11. S. Mandal, A. V. Marsh, H. Faber, et al., "A Robust Organic Hydrogen Sensor for Distributed Monitoring Applications," *Nature Electronics* 8 (2025): 343–352, https://doi.org/10.1038/s41928-025-01352-y.

12. Z. Chen, P. Yuan, C. Chen, et al., "Balancing Pd–H Interactions: Thiolate-Protected Palladium Nanoclusters for Robust and Rapid Hydrogen Gas Sensing," *Advanced Materials* 36 (2024): 2404291, https://doi.org/10.1002/adma.202404291.

13. M.-S. Jo, K.-H. Kim, J.-S. Lee, et al., "Ultrafast (~0.6 s), Robust, and Highly Linear Hydrogen Detection Up to 10% Using Fully Suspended Pure Pd Nanowire," *ACS Nano* 17 (2023): 23649–23658, https://doi.org/10.1021/acsnano.3c06806.

14. Y. J. Kim, S. Lee, S. Choi, et al., "Highly Durable Chemoresistive Micropatterned PdAu Hydrogen Sensors: Performance and Mechanism," *ACS Sensors* 9 (2024): 5363–5373, https://doi.org/10.1021/acssensors.4c01599.

15. R. Nagpal, M. Sugihara, N. Magariu, et al., "Humidity-Tolerant Selective Sensing of Hydrogen and n-Butanol Using ZIF-8 Coated CuO:Al Film," *Materials Chemistry Frontiers* 9 (2025): 3425–3442, https://doi.org/10.1039/D5QM00565E.

16. V. Postica, O. Lupan, A. Gapeeva, et al., "Improved Long-Term Stability and Reduced Humidity Effect in Gas Sensing: SiO_2 Ultra-Thin Layered ZnO Columnar Films," *Advanced Materials Technologies* 6 (2021): 2001137, https://doi.org/10.1002/admt.202001137.

17. R. Nagpal, M. Sugihara, C. Lupan, et al., "ZIF-71-Coated CuO:Al With Enhanced Gas-Sensing Performance for n-Butanol and Hydrogen," *ACS Applied Electronic Materials* 7 (2025): 10198–10215, https://doi.org/10.1021/acsaelm.5c01659.

18. J. Hu, T. Xu, L. Jin, et al., "Two-Dimensional Hybrid SnO_2@ WO_3 Nanosheets Synthesized by Polyoxometallate Cluster–Nucleus Coassembly for Highly Efficient H_2 Detection," *ACS Sensors* 10 (2025): 7810.

19. Q. Hu, P. Solomon, L. Österlund, and Z. Zhang, "Nanotransistor-Based Gas Sensing With Record-High Sensitivity Enabled by Electron Trapping Effect in Nanoparticles," *Nature Communications* 15 (2024): 5259, https://doi.org/10.1038/s41467-024-49658-3.

15214095, 0, Downloaded from https://advanced.onlinelibrary.wiley.com/doi/10.1002/adma.75476 by Long Luo - University Of Utah J. Willard Marriott Library , Wiley Online Library on [27/10/2026]. See the Terms and Conditions (https://onlinelibrary.wiley.com/terms-and-conditions) on Wiley Online Library for rules of use; OA articles are governed by the applicable Creative Commons License

20. Y. Guo, Z. Yuan, J. Liang, et al., "Mechanistic Modeling and Experimental Demonstration of Pd-Catalyzed Dual-Gate TeSeO FET Hydrogen Sensors," *Sensors and Actuators B: Chemical* 447 (2026): 138779, https://doi.org/10.1016/j.snb.2025.138779.

21. X. Geng, S. Li, J. Heo, et al., "Grain-Boundary-Rich Noble Metal Nanoparticle Assemblies: Synthesis, Characterization, and Reactivity," *Advanced Functional Materials* 32 (2022): 2204169, https://doi.org/10.1002/adfm.202204169.

22. I. A. Kalinin, I. V. Roslyakov, D. Bograchev, et al., "High Performance Microheater-Based Catalytic Hydrogen Sensors Fabricated on Porous Anodic Alumina Substrates," *Sensors and Actuators B: Chemical* 404 (2024): 135270, https://doi.org/10.1016/j.snb.2023.135270.

23. K. Bao, S. Qiu, W. Wang, et al., "Durable Carrier-Free Catalytic Combustion H_2 Sensor Based on PdPt Alloy Nanoparticles," *International Journal of Hydrogen Energy* 138 (2025): 28–35, https://doi.org/10.1016/j.ijhydene.2025.05.020.

24. H. M. Luong, M. T. Pham, T. Guin, et al., "Sub-Second and ppm-Level Optical Sensing of Hydrogen Using Templated Control of Nano-Hydride Geometry and Composition," *Nature Communications* 12 (2021): 2414, https://doi.org/10.1038/s41467-021-22697-w.

25. A. Theodoridis, C. Andersson, S. Nilsson, J. Fritzsche, and C. Langhammer, "A Catalytic-Plasmonic Pt Nanoparticle Sensor for Hydrogen Detection in High-Humidity Environments," *ACS Sensors* 10 (2025): 8983.

26. Z. Liu, C. Wang, Y. Yang, et al., "Reconfigurable Flexible Plasmonic Hydrogen Sensor Based on Disordered Palladium Nanoparticles: Coupled Optical Modulation and 3D Structural Rearrangement," *ACS Sensors* 10 (2025): 6859.

27. Grand View Research, Catalytic - Gas Sensor Market Outlook, https://www.grandviewresearch.com/horizon/statistics/gas-sensor-market/technology/catalytic/global.

28. D. Del Orbe Henriquez, I. Cho, H. Yang, et al., "Pt Nanostructures Fabricated by Local Hydrothermal Synthesis for Low-Power Catalytic-Combustion Hydrogen Sensors," *ACS Applied Nano Materials* 4 (2021): 7.

29. B. Xie, Y. Liu, Y. Lei, et al., "Innovative Thermocatalytic H_2 Sensor With Double-Sided Pd Nanocluster Films on an Ultrathin Mica Substrate," *ACS Sensors* 9 (2024): 2529.

30. I. I. Ivanov, A. M. Baranov, V. A. Talipov, et al., "Investigation of Catalytic Hydrogen Sensors With Platinum Group Catalysts," *Sensors and Actuators B: Chemical* 346 (2021): 130515, https://doi.org/10.1016/j.snb.2021.130515.

31. International Organization for Standardization, Hydrogen Detection Apparatus—Stationary Applications, ISO 26142:2010, International Organization for Standardization, Geneva, Switzerland, 2010.

32. V. Palmisano, E. Weidner, L. Boon-Brett, et al., "Selectivity and Resistance to Poisons of Commercial Hydrogen Sensors," *International Journal of Hydrogen Energy* 40 (2015): 11740–11747, https://doi.org/10.1016/j.ijhydene.2015.02.120.

33. E.-B. Lee, I.-S. Hwang, J.-H. Cha, et al., "Micromachined Catalytic Combustible Hydrogen Gas Sensor," *Sensors and Actuators B: Chemical* 153 (2011): 392–397, https://doi.org/10.1016/j.snb.2010.11.004.

34. L. Boon-Brett, J. Bousek, G. Black, et al., "Identifying Performance Gaps in Hydrogen Safety Sensor Technology for Automotive and Stationary Applications," *International Journal of Hydrogen Energy* 35 (2010): 373–384, https://doi.org/10.1016/j.ijhydene.2009.10.064.

35. J. M. Smith, "Introduction to Chemical Engineering Thermodynamics," *Journal of Chemical Education* 27 (1950): 584, https://doi.org/10.1021/ed027p584.3.

36. W. Kim, B. Jang, H.-S. Lee, and W. Lee, "Reliability and Selectivity of H_2 Sensors Composed of Pd Film Nanogaps on an Elastomeric Substrate," *Sensors and Actuators B: Chemical* 224 (2016): 547–551, https://doi.org/10.1016/j.snb.2015.10.092.

37. L. T. Duy, R. Yeasmin, S.-I. Han, S. Iqbal, C. Park, and H. Seo, "Chemiresistive Hydrogen Sensors Using a Pd-Ni Nanocatalyst and a TiOx/PTFE Humidity Passivation," *Sensors and Actuators B: Chemical* 394 (2023): 134387, https://doi.org/10.1016/j.snb.2023.134387.

38. D. Tomeček, H. K. Moberg, S. Nilsson, et al., "Neural Network Enabled Nanoplasmonic Hydrogen Sensors With 100 Ppm Limit of Detection in Humid Air," *Nature Communications* 15 (2024): 1208.

39. J. Ning, X. Zhu, T. Hu, et al., "Hydrogen Incorporation Selectively Modulates the Catalytic Performance of Pd Nanozymes for Cascade-Catalytic Tumor Therapy," *Journal of the American Chemical Society* 147 (2025): 15519–15533, https://doi.org/10.1021/jacs.5c02114.

40. K. A. U. Madhushani, H. Park, H. Zhou, et al., "Σ3(111) Grain Boundaries Accelerate Hydrogen Insertion Into Palladium Nanostructures," *Nano Letters* 25 (2025): 15215–15223, https://doi.org/10.1021/acs.nanolett.5c03431.

41. R. G. Mariano, K. McKelvey, H. S. White, and M. W. Kanan, "Selective Increase in CO_2 Electroreduction Activity at Grain-Boundary Surface Terminations," *Science* 358 (2017): 1187–1192, https://doi.org/10.1126/science.aao3691.

42. S. K. M. Padavala, S. Nimasha, K. A. U. Madhushani, et al., "Subsurface Hydrogen, Curvature, and Strain: Lessons from Electro-Reduction of Benzaldehyde on Nano-Structured Pd Catalysts," *Journal of Materials Chemistry A* 13 (2025): 31770–31780, https://doi.org/10.1039/D5TA05129K.

43. X. Yin, C. Wei, C. Tang, et al., "H-Embedding Induced Electron Localization in Pd Lattice for Improving Electrochemical Hydrogen Purification," *Small Methods* 9 (2025): 2500249, https://doi.org/10.1002/smtd.202500249.

44. rJ. F. Moulder, W. F. Stickle, P. E. Sobol, and K. D. Bomben, Handbook of X-ray Photoelectron Spectroscopy (Ed.: J. Chastain), Perkin-Elmer Corporation, Eden Prairie, MN, USA, 1992.

45. O. Lupan, V. Postica, M. Hoppe, et al., "PdO/PdO_2 Functionalized ZnO : Pd Films for Lower Operating Temperature H 2 Gas Sensing," *Nanoscale* 10 (2018): 14107–14127, https://doi.org/10.1039/C8NR03260B.

46. W. J. Buttner, "Standard Hydrogen Test Protocols for the NREL Sensor Testing Laboratory," *National Renewable Energy Laboratory*, Golden, CO, USA, 2011, https://doi.org/10.2172/1032663.

47. S. Syrenova, C. Wadell, F. A. A. Nugroho, et al., "Hydride Formation Thermodynamics and Hysteresis in Individual Pd Nanocrystals With Different Size and Shape," *Nature Materials* 14 (2015): 1236–1244, https://doi.org/10.1038/nmat4409.

Supporting Information

Additional supporting information can be found online in the Supporting Information section.

Supporting File: adma75476-sup-0001-SuppMat.pdf.

15214095, 0, Downloaded from https://advanced.onlinelibrary.wiley.com/doi/10.1002/adma.75476 by Long Luo - University Of Utah J. Willard Marriott Library , Wiley Online Library on [27/10/2026]. See the Terms and Conditions (https://onlinelibrary.wiley.com/terms-and-conditions) on Wiley Online Library for rules of use; OA articles are governed by the applicable Creative Commons License